SCIENCE CHINA
Technological Sciences

•Article•

January 2022 Vol.65 No.1: 41–52
https://doi.org/10.1007/s11431-021-1918-8

Effects of laser processing parameters on properties of laser-induced graphene by irradiating CO_2 laser on polyimide

LIU Ming[1,2*], WU JiaNan[1,2] & CHENG HuanYu[3,4*]

[1] *School of Mechanical Engineering and Automation, Fuzhou University Qishan Campus, Fuzhou 350116, China;*
[2] *State Key Laboratory of Digital Manufacturing Equipment and Technology, School of Mechanical Science and Engineering, Huazhong University of Science and Technology, Wuhan 430074, China;*
[3] *Department of Engineering Science and Mechanics, The Pennsylvania State University, University Park PA 16802, USA;*
[4] *Department of Materials Science and Engineering, The Pennsylvania State University, University Park PA 16802, USA*

Received June 21, 2021; accepted August 10, 2021; publlished online December 6, 2021

The emerging technique of carbonization of polyimide (PI) by direct laser writing receives great attention for its flexibility, versatility, and ease-of-patterning capability in creating a variety of functional laser-induced graphene (LIG) sensors and devices. LIG prepared by CO_2 laser irradiating of the PI film is characterized by scanning electron microscopy (SEM), X-ray diffraction (XRD), transmission electron microscope (TEM), specific surface area analyzer, synchronous thermal analysis, and Raman spectroscopy with the focus on investigating the effects of laser parameters (e.g., power, scanning speed) on the microstructure, thickness, and sheet resistance of LIG. Both TEM and XRD indicate that LIG is composed of many graphene layers with a layer spacing of 0.34 nm. The specific surface area of LIG decreases with the increase of laser power. The ratio of the thickness of LIG over the depth of the carbonized PI film as the expansion ratio characterizes the expansibility of LIG. The influence of image resolution and off-focus value on the sheet resistance of LIG is explained by the superposition mechanism of laser scanning spots.

CO_2 laser, laser parameters, laser-induced graphene, characterization, sheet resistance

Citation: Liu M, Wu J N, Cheng H Y. Effects of laser processing parameters on properties of laser-induced graphene by irradiating CO_2 laser on polyimide. Sci China Tech Sci, 2022, 65: 41–52, https://doi.org/10.1007/s11431-021-1918-8

1 Introduction

Graphene, which is a single-layer two-dimensional material with a honeycomb lattice of carbon atoms, has a wide application potential in material science [1–4] due to its unique lattice structure and excellent properties such as high surface area (2630 $m^2 g^{-1}$) [5], large thermal conductivity (3000 $W m^{-1} K^{-1}$) [6], high light transmittance (visible and near-infrared absorption of 2.3%) [7], good chemical stability [8] and biocompatibility [9]. Three-dimensional porous graphene is of versatility in the field of flexible electronic devices with its unique physical and chemical properties being capable of meeting the requirements of most flexible devices, and has become a research hotspot in recent decades [10–15]. Three-dimensional porous graphene has been mainly prepared by chemical vapor deposition (CVD) [16–18], but its scalability is limited [19] since the metal substrate has to be etched. In contrast, the treatment of functionalized graphene solution [20–22] is relatively more economical and scalable since porous graphene coatings can be prepared on various substrates. However, additional patterning steps are required to obtain patterned structures designed specifically to meet the requirements of flexible electronic devices [23]. Economically and environmentally friendly preparation

*Corresponding authors (email: mingliu@fzu.edu.cn; Huanyu.Cheng@psu.edu)

processing of three-dimensional porous graphene is a challenge for the development of flexible electronic devices [24–29].

Laser technology, which is non-contact, non-toxic, and highly controllable, can achieve higher precision of thermal induction compared with conventional thermal methods, and has been widely used in material processing and manufacturing, medical treatment, and military instruments [30–33]. The basic working principle of laser technology is the photothermal effect and photochemical effect produced by the interaction between laser and material with its unique one-step laser scribing process being highly promising for a wide range of applications including micro-supercapacitors [34–41], sensors [26,42–45], photodetectors [46], water treatment interfaces [47], and electrocatalysts [48]. Laser-induced graphene (LIG), which is known as three-dimensional porous graphene and can be used as sensitive or electrode material in flexible electronic devices due to its high specific surface area (340 m^2/g), high thermal stability under high temperature (> 900°C) and excellent electrical conductivity (5–25 S/cm). Prepared by CO_2 laser ablation of the precursor polyimide (PI) film in the atmosphere [33,34,49–51], the conductive, highly porous three-dimensional LIG with programmable patterns is easily functionalized to form LIG composites with metals, catalytic nanoparticles, aptamer or enzyme for biosensors, micro-supercapacitors, and radiofrequency devices [52–55]. Porous graphene can also be prepared on wood, which expands the material range of precursor, in Ar or H_2 atmosphere by multiple scanning of variable laser focal lengths [48]. Nitrogen-doped graphene thin films were successfully prepared by laser irradiation of graphite oxide in the NH_3 atmosphere [56]. A simple, controllable, and low-cost preparation method of LIG modified by manganese dioxide (LIG/MnO_2) was proposed on the basis of laser direct printing technology with good performance of supercapacitor LIG/MnO_2 [36]. Any material of high carbon can be transformed into porous graphene by laser processing in an inert atmosphere, provided that the energy density of laser processing reaches a critical threshold [48].

In this work, LIG was prepared by CO_2 laser irradiating PI in the atmosphere with the focus on investigating the influence of laser processing parameters (e.g., laser power, scanning speed, off-focus value, scanning pass, and imported image resolution) on properties of LIG (e.g., thickness, morphology, microstructure, and sheet resistance). LIG was characterized by scanning electron microscopy (SEM), X-ray diffraction (XRD), transmission electron microscope (TEM), specific surface area analyzer, synchronous thermal analysis, and Raman spectroscopy. The influence of laser scanning speed and off-focus value on the sheet resistance of LIG was discussed by the superposition mechanism of laser scanning spots.

2 Material preparation and characterization

A laser engraving and cutting system (MUSE) equipped with a CO_2 laser of wavelength λ = 10.6 μm was used for fabricating LIG under different conditions by varying laser power P, scanning speed v, repeated scanning pass n, image resolution, and off-focus value Δf. PI film of thickness 125 μm was irradiated by a CO_2 laser in a continuous mode. Large laser power can cause excessive carbonization of PI. Scanning speed, v, can be adjusted by the software RetinaEngrave 2.0, and the maximum value is 400 mm/s. The resolution of the imported scanning pattern needs to be converted, and only three resolutions are available in the RetinaEngrave 2.0, namely 250 × 250 dpi, 500 × 500 dpi, and 1000 × 1000 dpi. The distance of adjacent laser scanning lines is controlled by image resolution. Both image resolution of pre-designed patterns imported and laser scanning pass, n, affect sheet resistance of LIG. The rastering image used in the experiment is a rectangular solid area with an aspect ratio of 3:1 drawn by AutoCAD. The off-focus value, Δf, ranging from −3 to 3 mm was used to study the influence of spot diameter on the sheet resistance of LIG considering the Gaussian characteristics of the CO_2 laser beam.

Scanning electron microscopy (SEM) was performed by Quanta 250 to examine the microstructure of LIG processed under different conditions of laser irradiation. Raman spectroscopy was carried out by Invia Reflex Raman microscope with the excitation laser source emitting 10% of full power at a wavelength of 532 nm. X-ray diffraction (XRD) was conducted on LIG, which was carefully scraped off from PI to avoid the influence of PI, by a polycrystalline diffractometer DY5261/Xpert3 with Cu K_α radiation (λ = 1.54 Å). Transmission electron microscopy (TEM) and high-resolution TEM (HRTEM) images were obtained using a TECNAI G2 F20 field emission gun transmission electron microscope. TEM samples were prepared by scratching LIG from PI substrate, followed by sonication in alcohol, and dropping the slurry onto a lacey carbon copper grid. The surface area of LIG was measured with a specific surface area and porosity analyzer ASAP2460, and the powder samples were degassed at a temperature of 300°C for 6 h before the test. Synchronous thermal analysis was carried out by TG Instruments STA449C analyzer (10°C min^{-1} from 29 to 1000°C in nitrogen) in order to characterize carbonization degradation temperature of PI and thermal stability of LIG. Three-dimensional morphologies of LIG and the intact region of PI film after the removal of LIG were characterized by the laser confocal microscope (OLYMPUS FV3000). Due to the dependence of sheet resistance R of LIG on the size of graphene, the laser scanning area was fixed to be 18 mm × 6 mm. Resistance R_m, from which sheet resistance R can be calculated ($R = R_m W/L$, W and L are the width and length of LIG film, and W = 6 mm, L = 18 mm in the current

study), was measured by voltammetry (Keithley 2450 digital source meter) with copper tapes and copper wires leading out electrodes. The influence of the contact resistance on the measurement of resistance is ignored, since the contact resistance between the metal wires and LIG is far less (about 1%) than the internal resistance of LIG [57].

3 Results and discussion

Figure 1(a)–(d) show scanning electron microscopy (SEM) of LIG obtained at four different powers (i.e., 7.2, 9, 10.8, and 12.6 W). Under a small power of 7.2 W in Figure 1(a), the surface morphology of LIG is uniform and smooth with grooves caused by the linear scanning of the laser. LIG is of a porous structure like foam, whose porosities are created by the gas that is generated by the recombination of heteroatoms [34,35]. When the laser power reaches 9 W, fibrous clusters appear at the overlapping domains of the adjacent scanning lines (Figure 1(b)), leading to the secondary carbonization and structure change of LIG. Most of the region is still porous under 9 W, and the pores under 9 W are larger than those under 7.2 W, indicating that the microstructure can be controlled by laser power. When the laser power reaches 10.8 W in Figure 1(c), the fibrous cluster material extends to the whole surface. The thickness of LIG further increases with the increasing laser power, as observed in the cross-sectional images in Figure 1(e)–(h). With the increase of laser power to P = 12.6 W in Figure 1(d), fiber bundles are formed and entangled with one another to form a network structure with the whole surface being covered by fiber bundles in the absence of porous graphene. The diameters of laser-induced fiber bundles under 12.6 W are larger than those under 10.8 W. The structure of LIG can change from porous foam to fibrous structure bundles with the increase in laser power, which is consistent with the previous literature report [35].

Figure 2(a) shows Raman spectra of precursor PI and LIG prepared at different powers (5.4, 7.2, 9, 10.8, and 12.6 W). PI has no characteristic peak in the Raman spectra, but LIG has three characteristic peaks: (1) D peak at about 1350 cm^{-1} is the disordered vibration peak of graphene [58] to characterize defect of graphene; (2) G peak near 1580 cm^{-1} comes from E_{2g} mode of double degenerate center [59] to characterize the symmetry and order of graphene; and (3) 2D peak at about 2695 cm^{-1} as in the single-layer graphene [60] is the second-order Raman peak of double phonon resonance to reflect the stacking mode of carbon atom layers [61]. With the increase of laser power, the intensity and half-width of the characteristic peaks vary, but the Raman shift remains unchanged, demonstrating that LIG is successfully generated under the power range used in this study. The intensity ratios I_D/I_G and I_{2D}/I_G of LIG prepared at different powers indicate that defect density and carbon atom stacking mode of graphene vary with laser power (Figure 2(b)). The characteristic peak intensity "I" is calculated by integrating the peak area, and the subscript indicates the specific peak (D, 2D, or G). The intensity ratio, I_D/I_G, reflects the defect density: a larger I_D/I_G corresponds to a larger defect density of LIG. With the increase of laser power, I_D/I_G decreases first and then increases, consisting with the previously reported result [34]. When the laser power is 9 W, I_D/I_G is the minimum (about 0.6), indicating that the graphene defects are the fewest. With the increase in laser power, PI is further carbonized with more generation of LIG and more pores caused by the gas channeling, and LIG can be transformed from porous structure to fibrous bundles. The carbonized degree of PI and creation of pores are two competing mechanisms influencing the defect density of LIG: a higher extent of carbonization improves the stability of LIG, resulting in reduction of defects; while excessive power makes more pores, and LIG can transform from porous structure to fibrous bundles, resulting in the increase of defects, which is demonstrated by the increase in I_D/I_G. The number of graphene layers can be quantitatively characterized by I_{2D}/I_G: a larger I_{2D}/I_G indicates fewer graphene layers. With the increase of laser power, the peak intensity ratio I_{2D}/I_G decreases gradually, from 1.16 at 5.4 W to 0.86 at 12.6 W, which is caused by the recombination of some suspended bonds, dopants, and defect atoms in graphene due to thermal effect, making LIG with more fibrous bundles become more symmetrical and ordered with more layers [62].

The XRD patterns of LIG prepared under two different powers (5.4 W and 10. 8 W) exhibit the prominent peak 2θ = 25.9° (Figure 3(a)) that corresponds to (002) plane of LIG [35]. The layer spacing l of LIG can be obtained as l = 3.42 Å by Bragg formula $n\lambda = 2l\sin\theta$ (λ = 1.54 Å is the wavelength of X-ray, θ = 12.95° is the incident contact angle, n =1 for the first-order diffraction), indicating that LIG has a high degree of graphitization. The peak at 2θ = 47° is indexed to (100) reflections that are associated with in-plane structure [34,63], and is not obvious and only slightly seen.

LIG prepared at 5.4 W has good thermal stability and high graphitization degree (Figure 3(b)), since the weight of LIG decreases slightly below 1000°C with the small change due to the evaporation of water and the pyrolysis of internal impurities in LIG. Under low temperature (< 550°C), the weight of the precursor material PI decreases slightly with the subtle decrease being caused by dehydration, indicating good heat stability of PI. Under temperatures larger than 550°C, the pyrolysis becomes prominent, and PI can be carbonized as in the previous results [63]. Successful preparation of LIG requires a sufficiently large temperature, which is controlled by laser power. PI cannot be carbonized under small power, under which the required temperature cannot be met.

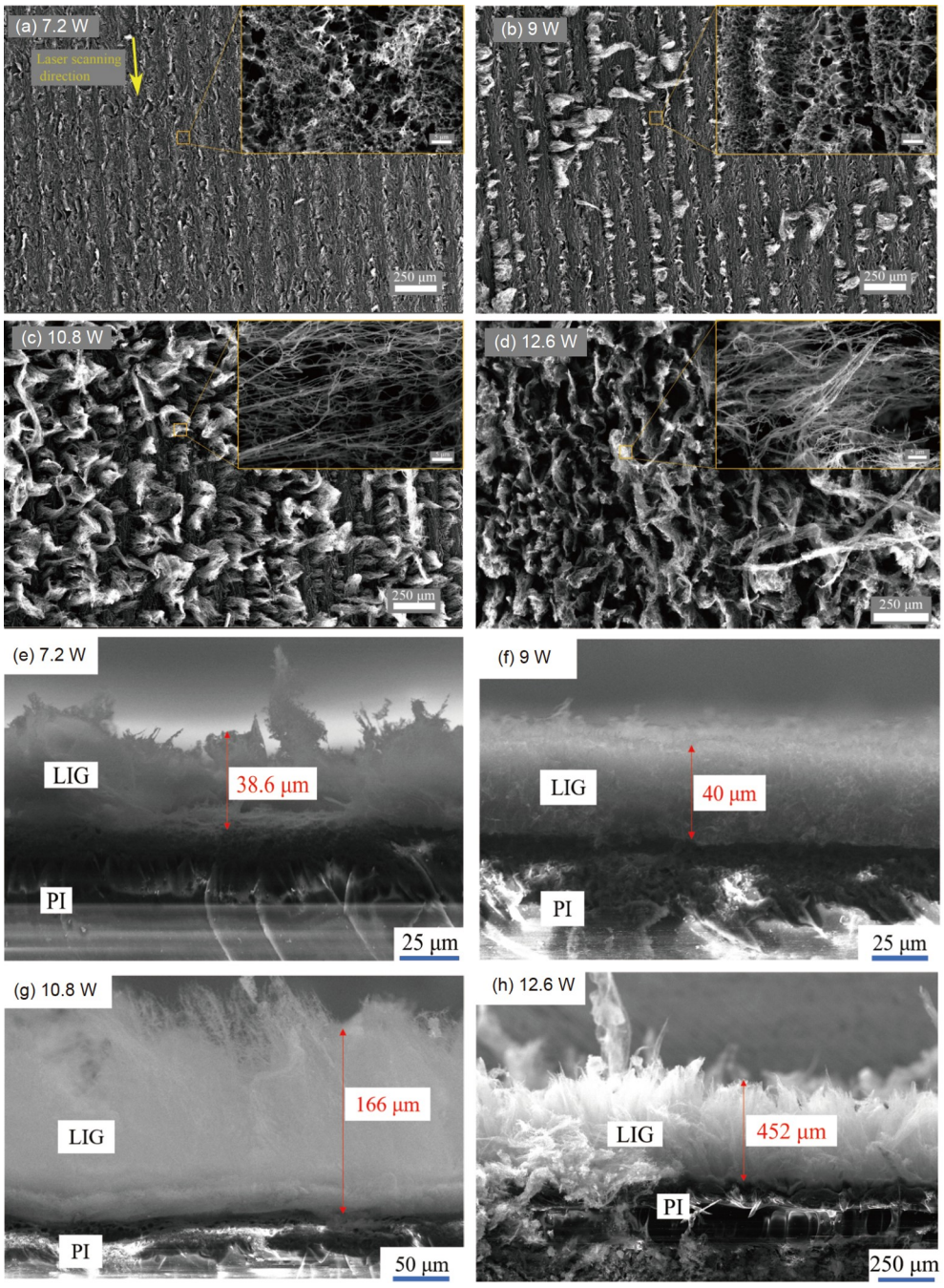

Figure 1 (Color online) Scanning electron microscope (SEM) images of LIG at different powers (scanning speed v = 160 mm/s, image resolution 1000×1000 dpi, off-focus value Δf = 0, scanning pass n = 1). (a) 7.2; (b) 9; (c) 10.8; (d) 12.6 W; (e)–(h) are cross-sectional images of LIG prepared at 7.2, 9, 10.8 and 12.6 W, respectively.

Transmission electron microscopy (TEM) images of LIG prepared by two different laser powers 7.2 and 10.8 W also confirm the observations from XRD and SEM (Figure 4). LIG prepared at 7.2 W is lamellar and similar to the thin silk towel with curl (Figure 4(a)). The high-resolution image of the edge shows that LIG is composed of many graphene layers with layer spacing of 0.34 nm, which is consistent with the layer spacing (i.e., 0.342 nm) obtained by the Bragg formula from the XRD pattern. The LIG obtained at P = 10.8 W is fibrous (Figure 4(b)), which is also consistent with the observation of SEM. Under high laser power (e.g., P = 10.8 W) to induce high temperature, the lamellar LIG is further pyrolyzed, cracked, and curled into fibrous tubes. The high-resolution image of the edge of the fibrous LIG shows that it is still composed of many graphene layers with the same layer spacing of 0.342 nm, and the layer arrangement is more ordered.

The specific surface area of LIG can be obtained from

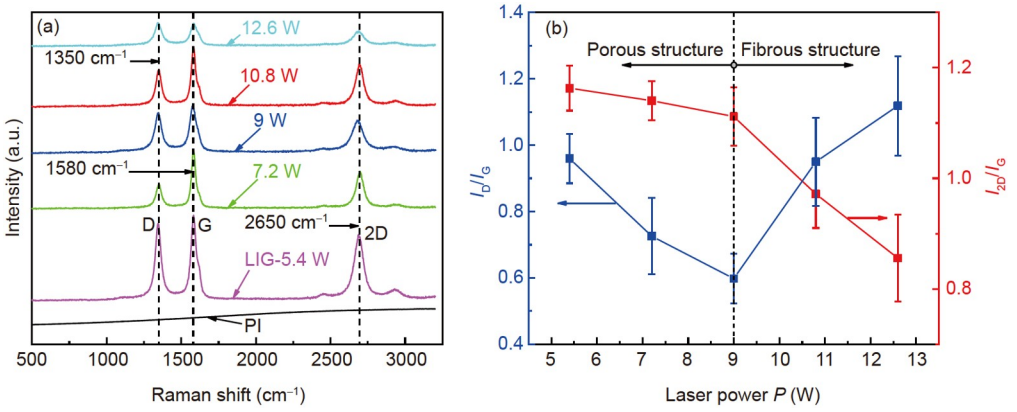

Figure 2 (Color online) (a) Raman spectra of precursor PI and LIG prepared at different powers (scanning speed v = 160 mm/s, image resolution 1000×1000 dpi, off-focus value Δf = 0, scanning pass n = 1); (b) analysis of D, 2D, and G peak intensities of Raman spectra of LIG.

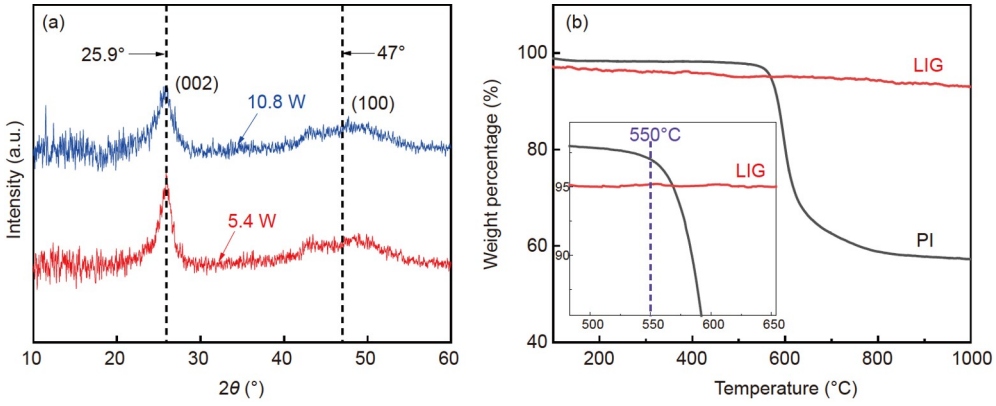

Figure 3 (Color online) X-ray diffraction (XRD) analysis and thermogravimetric analysis (TGA) (scanning speed v= 160 mm/s, image resolution 1000×1000 dpi, off-focus value Δf = 0, scanning pass n = 1). (a) XRD of LIG scraped from PI film at 5.4 and 10.8 W; (b) TGA of LIG prepared at 5.4 W and PI substrate under argon.

adsorption and desorption curves of LIGs (Figure 5(a) for 7.2 and 10.8 W) by Brunauer-Emmett-Teller (BET) method [64]. The adsorption and desorption curves of LIG do not coincide, and a hysteresis loop can be observed as in the previous study [65]. The specific surface area of LIG decreases with the increase of laser power, which makes the microstructure of LIG change from porous lamella to curly fibers. The specific surface area of LIG lies within the range from 70 [43] to 340 m^2/g [34] reported for laser-induced three-dimensional porous graphene, and is much smaller than that of the monolayer graphene of a single flake (i.e., 2630 m^2/g) [5]. Since laser power has an important influence on the specific surface area of LIG, the values of the specific surface area obtained under large laser powers ($\geq$ 7.2 W) in the present study are reasonably smaller than that (i.e., 340 m^2/g) obtained under a small laser power of 3.6 W [34].

The dependence of sheet resistance R of LIG on laser power P is investigated by the experimental setup in Figure 6(a). After the measurement of resistance R_m from Keithley digital source meter, sheet resistance R can be obtained as $R = R_m W/L$, where W and L are the width and length of LIG film (W = 6 mm, L = 18 mm in the current study). Since the transformation of PI film into porous graphene by laser processing requires that the energy density of laser processing reaches a critical threshold, LIG cannot be prepared under small laser power, which is indicated by the extremely large resistance (> 40 MΩ). The sheet resistance R decreases linearly with the increase of laser power P as in the previous study [34]. The basic principle of preparing porous graphene by laser direct writing is the photothermal effect of laser radiation on the surface of PI. The unit energy density increases with the increase of laser power, causing further carbonization of PI, which leads to the decrease of sheet resistance. LIG of fibrous microstructure also possesses more contact points or electrically conductive pathways to result in decreased sheet resistance compared to LIG of porous microstructure under the same image resolution. The ordered structure of LIG would be destroyed when P > 15 W, under which sheet resistance would become larger, and macroscopically visible fibrous bundles can suspend and drift in the air. Figure 6(b) presents the dependence of normalized resistance change $\Delta R/R_0$ ($\Delta R = R_0 - R$, R_0 and R

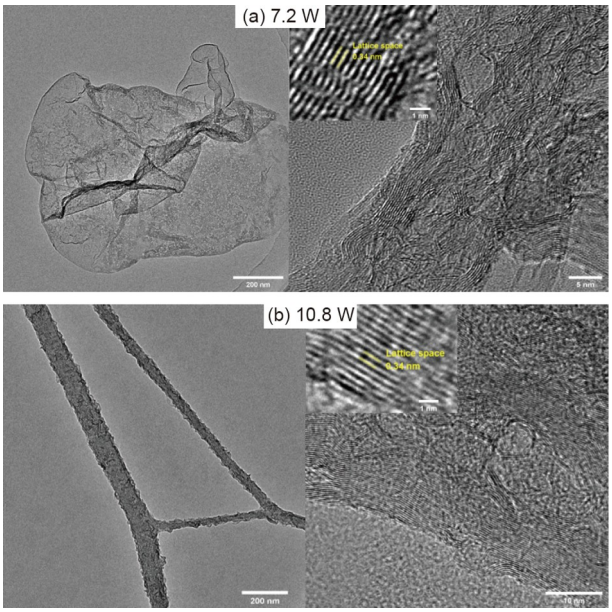

Figure 4 (Color online) Transmission electron microscopy (TEM) and (HRTEM) images of LIG prepared under two different laser powers (scanning speed v= 160 mm/s, image resolution 1000×1000 dpi, off-focus value Δf = 0, scanning pass n = 1). (a) 7.2 W; (b) 10.8 W.

represent sheet resistance before and after bending) of LIG on laser power P for different bending conditions (b = 12.5%, 25%). $\Delta R/R_0$ decreases with the increase of P, and a larger bending strain produces a greater change in $\Delta R/R_0$. However, the effect of bending on $\Delta R/R_0$ becomes negligibly small under large P, which can be explained by the theory of contact units [66]. In brief, LIG/PI composite can be regarded as particulate-filled heterogeneous material in nature. The conductivity depends on the number of contact points or electrically conductive pathways of adjacent carbon units. Higher laser power can produce more robust and tight contact carbon units (like fibrous structures), weakening the sensibility of LIG to bending strain.

The total thickness h_t of the prepared LIG can be divided into two parts with the upper part h_u above the original surface and the lower part h_l below the original surface, as shown in Figure 7(a). With the increase of laser power P, the total thickness h_t increases slowly in the power range of 6.3–9 W, and h_t increases sharply when the power becomes larger than 9.9 W. The two-stage variation of h_t with P can be explained by noting the microstructure change of LIG from porous structures to fibrous bundles. When the structure is porous under small P, the energy density absorbed by PI film increases with the increase of P, leading to the slow increase in h_l; when fibrous bundles form under high P, LIG will expand to a greater extent, resulting in the rapid increase in h_t with P. The expansion of LIG is very pronounced, and h_t can be several times the thickness (i.e., 125 μm) of the PI film, which is caused by thermal expansion and internal gas escape, especially under large laser power. A linear relationship between h_l and P can be approximated.

Figure 7(b) shows the height profile of the section line along scanning direction under laser power P = 11.7 W with the inset showing the three-dimensional (3D) image of the intact region of PI after removing LIG. The equidistant conical pits that correspond to the circular regions on the contour plot of the intact region are caused by the Gaussian beam characteristics of the laser. The edges of LIG are not perpendicular to the surface with the bending caused by the thermal-stress-induced deflection of PI film. The diameter of circular pits and the distance between conical pits depend on laser power, scanning velocity, and image resolution (the diameter of circular pits and the distance between adjacent conical pits are both about 80 μm at P = 11.7 W). The carbonization depth of the LIG is determined as the vertical distance between the surface of PI and the bottom of the laser carbonization layer that is revealed by removing LIG. The carbonization depth of 24 μm can be found for P = 11.7 W (Figure 7(b)) based on the three-dimensional image of the residual carbonization region by laser confocal microscope (OLYMPUS FV3000).

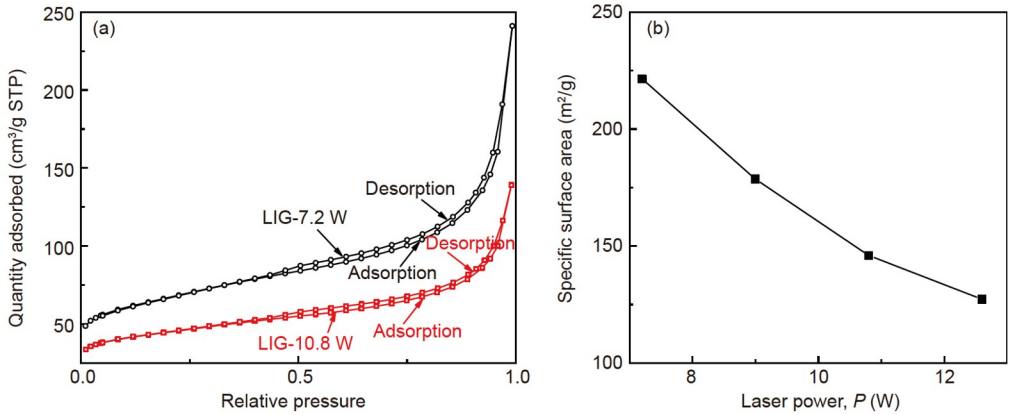

Figure 5 (Color online) (a) Adsorption/desorption curves of LIGs under 7.2 and 10.8 W; (b) the dependence of specific surface area on laser power. Scanning speed v = 160 mm/s, image resolution 1000×1000 dpi, off-focus value Δf = 0, scanning pass n = 1.

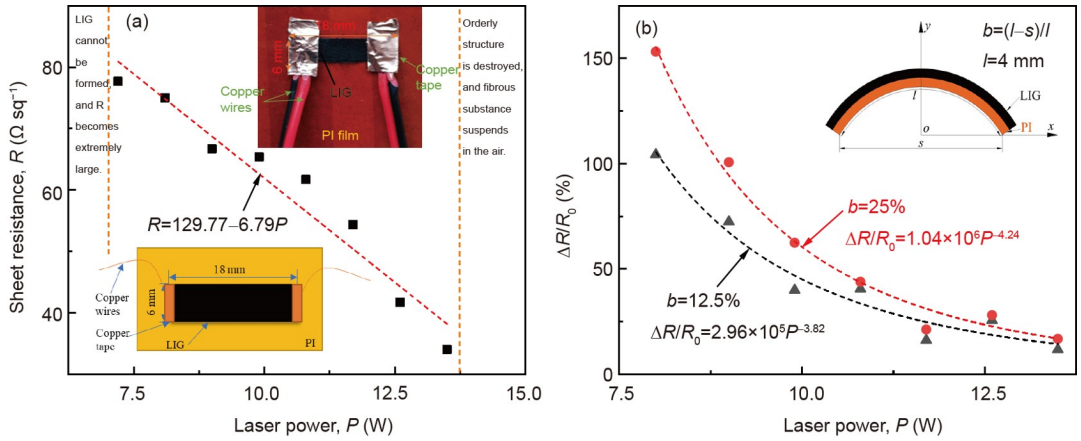

Figure 6 (Color online) Dependence of (a) sheet resistance R without bending and (b) normalized resistance change $\Delta R/R_0$ of LIG with bending on laser power P (scanning speed v = 400 mm/s, image resolution 1000×1000 dpi, off-focus value Δf = 0, scanning pass n = 1). The insets in (a) show the schematic illustration and the experimental setup for measuring resistance R_m of the LIG film. The inset in (b) shows the method of bending characterization.

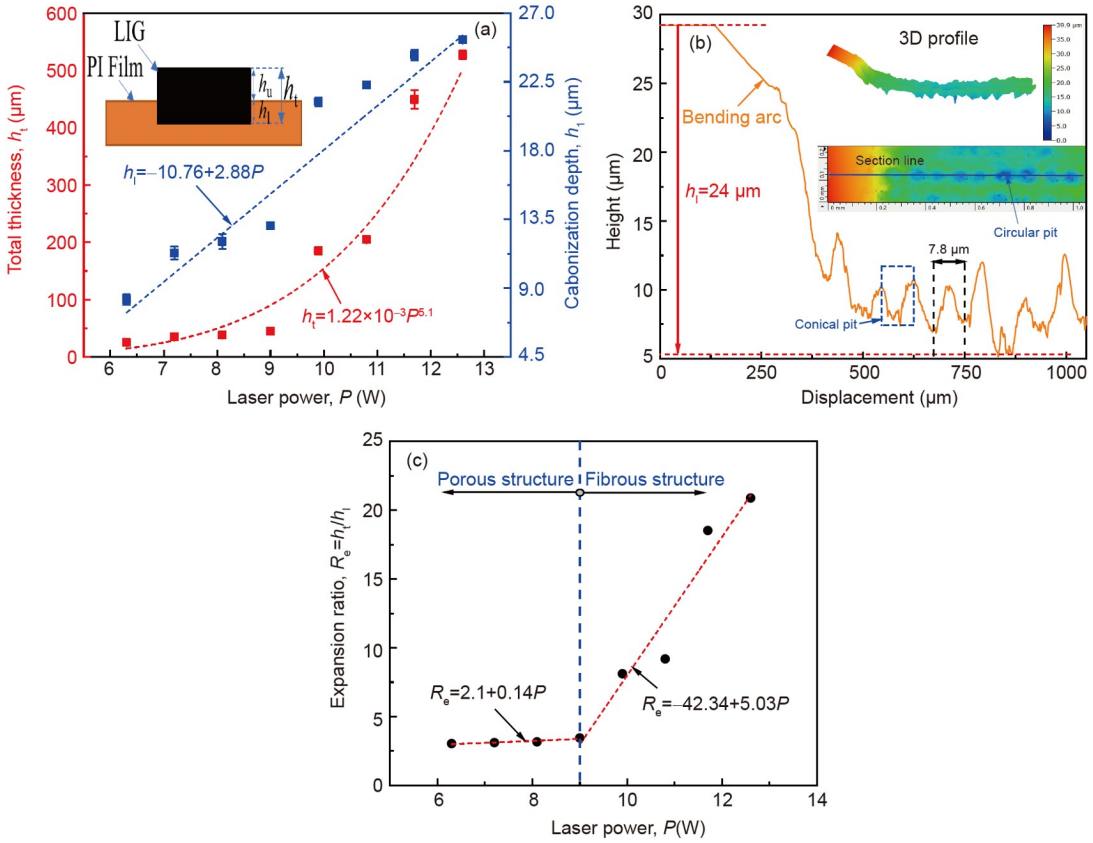

Figure 7 (Color online) Geometrical characterization of LIG (scanning speed v = 400 mm/s, image resolution 250 × 250 dpi, off-focus value Δf = 0, scanning pass n = 1). (a) Dependence of the carbonization depth h_l of PI and total thicknesses h_t of LIG film on laser power P, the inset shows the schematic illustration of h_l and h_t; (b) height profile of the section line on the intact region of PI after removing LIG under P = 11.7 W, the section line is along the scanning direction, the insets show the 3D and surface morphology of the intact region of PI after removing LIG; (c) dependence of expansion ratio $R_e = h_t/h_l$ on laser power P.

The expansion ratio $R_e = h_l/h_t$ characterizes the expansion extent of LIG (Figure 7(c)). The increase in laser power makes LIG expand and also causes the transformation of its microstructure. With the increase in laser power, the expansion ratio increases in a piecewise linear way: the linear fitting slope is 0.71 W^{-1} for porous structures (laser power range of 6.3–9 W) and 4.28 W^{-1} for fibrous bundles (laser power range of 9–12.6 W). Carbon material of high expansion ratio (e.g., conventional thermal reduction graphene oxide and laser reduced graphene oxide [65]) contains a porous structure for improved sensitivity and ion transport efficiency, which are suitable for sensing and storage of

electrolyte material as high capacitance supercapacitors. Since the expansion ratio (R_e > 20 at P = 12.6 W) of LIG prepared by laser carbonization of PI is much higher than that (about 3 [65]) of thermally reduced graphene oxide, LIG is more suitable for micro-supercapacitors and sensing.

A larger image resolution corresponds to a smaller distance between adjacent pixels, leading to a larger overlap area of adjacent laser spots that are assumed to be circular (inset, Figure 8). The overlap area A can be calculated as

$$A = 8\int_{q/2}^{d_0/2}\left(\sqrt{\frac{d_0^2}{4}-x^2}\right)\mathrm{d}x$$
$$= \frac{d_0^2}{2}\left(\pi-2\arcsin\frac{q}{d_0}-\frac{2q}{d_0^2}\sqrt{d_0^2-q^2}\right), \quad (1)$$

where d_0 is the laser spot diameter on the focal plane, q is the distance between the two adjacent laser beams, and x is along the scanning direction. The total energy E in a single circular area can be expressed as

$$E = E_0+\frac{A}{\pi(d_0/2)^2}E_0$$
$$= \left(1+\frac{4A}{\pi d_0^2}\right)E_0 = kE_0, \quad (2)$$

where E_0 is the energy emitted by a single laser beam; $4A/\left(\pi d_0^2\right)$ denotes the energy absorbed by the superimposed region, and k represents energy coefficient as

$$k = 1+\frac{2}{\pi}\left(\pi-2\arcsin\frac{q}{d_0}-\frac{2q}{d_0^2}\sqrt{d_0^2-q^2}\right). \quad (3)$$

With the increase of image resolution, the distance q between adjacent laser spots decreases from q = 78 μm for 250 × 250 dpi to q = 39 μm for 500 × 500 dpi and then to q = 19.5 μm for 1000 × 1000 dpi. With known laser spot diameter d_0 = 100 μm under Δf = 0, k calculated by eq. (3)

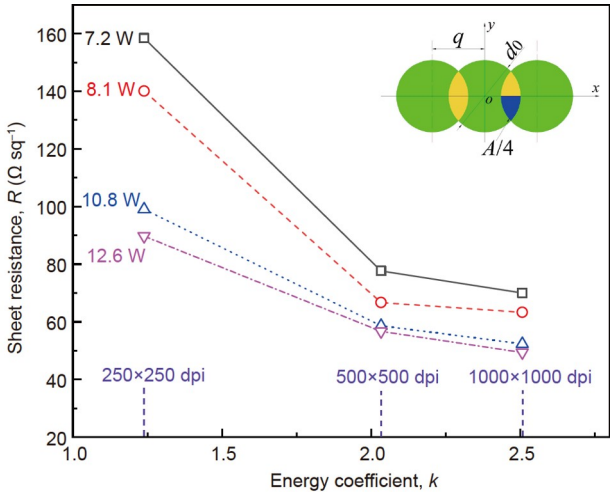

Figure 8 (Color online) Dependence of sheet resistance R of LIG on energy coefficient k (scanning speed v = 400 mm/s, off-focus value Δf = 0, scanning pass n = 1) with the inset showing the schematic diagram of laser spot superposition.

increases with the increase of image resolution from 1.239 to 2.033 and then to 2.507 as image resolution increases from 250 × 250 to 500 × 500 and then to 1000 × 1000 dpi. Larger k corresponds to larger laser energy contributing to more carbonization of the PI film. Therefore, sheet resistance R of LIG decreases with the increase in energy coefficient k (Figure 8), since more carbonization of PI can make LIG more electrically conductive. When k increases from 1.239 (image resolution of 250 × 250 dpi) to 2.033 (image resolution of 500 × 500 dpi), sheet resistance R decreases significantly, whereas R decreases slightly as k further increases from 2.033 to 2.507 (image resolution of 1000 × 1000 dpi). The carbonization of PI tends to saturate under large power, which is manifested by the small difference of R between 10.8 and 12.6 W. A larger image resolution prepares LIG of a denser microstructure, resulting in more conductive pathways, and thus smaller sheet resistance. The capacitor fabricated by the combination of fibrous LIG prepared at small image resolution and porous LIG prepared at large image resolution was found to have larger capacitance than LIG capacitor of pure porous structure [43].

Sheet resistance R of LIG increases with the increase of scanning speed v (Figure 9(a)). The significant influence of scanning speed on sheet resistance of LIG can be explained by noting that the scanning speed can affect the unit energy applied to the unit scanned area, since the processing time of thermal effect in a single circular scanning area increases with the decrease of scanning speed. PI film cannot be carbonized into LIG under high scanning speed (e.g., v > 160 mm/s for P = 5.4 W). R is more sensitive to v for small P (< 9 W), since the extent of carbonization is low under small P, resulting in a prominent effect of processing time or v on R.

Figure 9(b) shows the normalized resistance change $\Delta R/R_0$ of LIG as a function of laser scanning speed v for a bending strain of b = 12.5%. $\Delta R/R_0$ increases with the increase of v, and $\Delta R/R_0$ from a lower laser power (e.g., 7.2 W) is larger than that from a higher laser power (e.g., 12.6 W) for the same scanning speed. With the increase of laser radiation energy, the microstructure of LIG changes from porous structures to tighter and fibrous bundles, which weakens the sensitivity of sheet resistance on scanning speed.

Under three different P for the laser scanning pass $n \le 10$, sheet resistance R can be approximated to be constant when $n \ge 3$ (Figure 10 (a)). The variation of R under different P for $n \le 3$ exhibits a prominent decrease in R at n = 2 with a slight decrease at n = 3 (Figure 10(b)). The decrease in R for $n \le 3$ can be explained by noting that more scanning passes can make LIG more homogeneous and uniform with more carbonization of PI, while the little change of R for $n \ge 3$ is caused by the saturation of carbonization.

In the schematic diagram of the working area of the laser beam (Figure 11(a)), f represents focal length, L denotes the

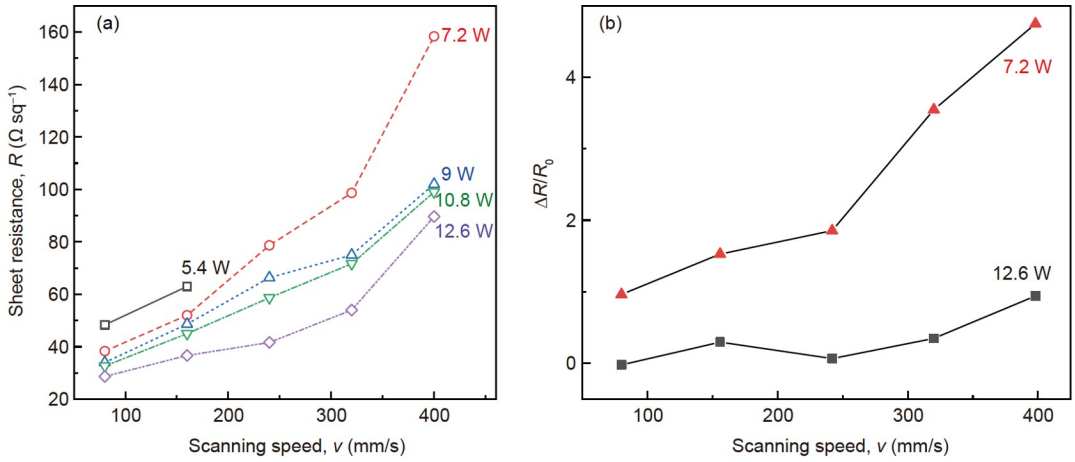

Figure 9 (Color online) Dependence of (a) sheet resistance R without bending and (b) normalized resistance change $\Delta R/R_0$ of LIG with bending (b = 12.5%) on laser speed scanning v (image resolution 250 × 250 dpi, off-focus value $\Delta f = 0$, and scanning pass n = 1).

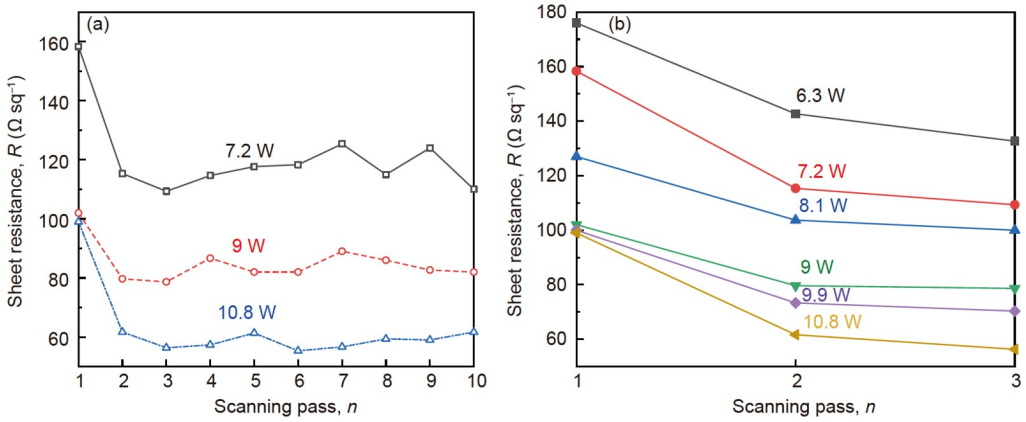

Figure 10 (Color online) Variation of sheet resistance R of LIG with scanning pass n (scanning speed v= 400 mm/s, image resolution 250×250 dpi, off-focus value off-focus value $\Delta f = 0$). (a) $n \leq 10$ under three different P; (b) $n \leq 3$ under different P.

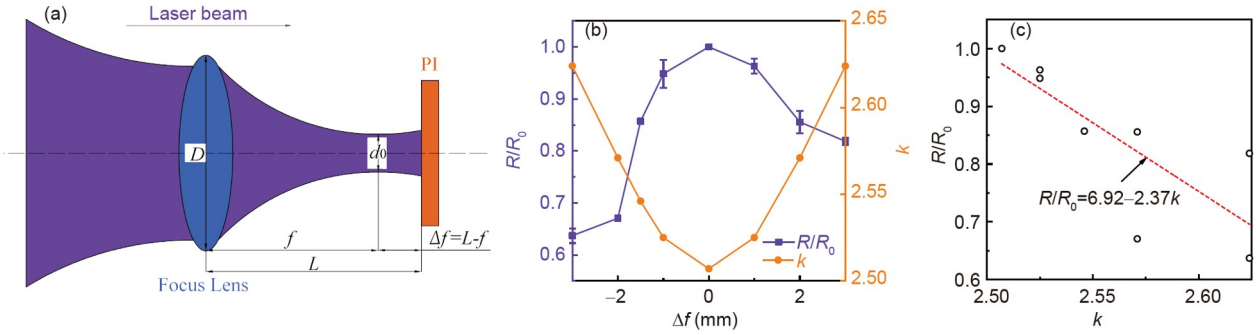

Figure 11 (Color online) Influence of off-focus value (laser power P = 9.9 W, scanning speed v = 400 mm/s, image resolution 1000×1000 dpi, scanning pass n = 1). (a) Schematic diagram of the working area of the laser beam; (b) dependence of normalized R (by R_0 at $\Delta f = 0$) and energy coefficient k by eq. (5) on off-focus value Δf; (c) dependence of R/R_0 on k.

distance between the focal lens and PI surface, and d_0 is the diameter of the laser spot on the focal plane. $\Delta f = L - f$ is off-focus value with positive defocus ($\Delta f > 0$) corresponding to the case that the focal plane is above the sample surface and negative defocus ($\Delta f < 0$) corresponding to the case that the focal plane is below the sample surface. The diameter d of the laser spot on the PI surface can be calculated according to Gaussian beam characteristics:

$$d = d_0\sqrt{1+\left(\frac{\Delta f}{f}\right)^2}, \tag{4}$$

where d increases with the increase of Δf. If the off-focus value is considered, d_0 should be changed to d in Eq. (3), so that the energy coefficient k can be expressed as

$$k = 1+\frac{2}{\pi}\left(\pi-2\arcsin\frac{q}{d_0\sqrt{1+\left(\frac{\Delta f}{f}\right)^2}}-\frac{2q}{d_0^2\left[1+\left(\frac{\Delta f}{f}\right)^2\right]}\sqrt{d_0^2\left[1+\left(\frac{\Delta f}{f}\right)^2\right]-q^2}\right), \tag{5}$$

where $q = 19.5$ μm for 1000 × 1000 dpi, $f = 3.5$ mm, and $d_0 = 100$ μm.

Figure 11(b) shows the dependence of the relative resistance R/R_0 (R is resistance considering off-focus value, and R_0 is the resistance at $\Delta f = 0$) and the energy coefficient k on off-focus value Δf. R/R_0 decreases with the increase of the absolute value of Δf, and R reaches the minimum value at zero off-focus value. Since both energy coefficient k and spot diameter d increase with the increase in the absolute value of Δf, a larger $|\Delta f|$ results in more carbonization of PI and more homogenous structure of LIG for a smaller sheet resistance. In the case of negative defocus ($\Delta f < 0$), the maximum energy density surface (i.e., the focal plane) is located in the interior of the sample [67], making the carbonization process start from the interior of PI, which is the reason why the resistance decreases more sharply for $\Delta f < 0$ than that for $\Delta f > 0$, under which condition the focal plane is above the PI surface. A linear relationship between R/R_0 and k can be approximated as shown in Figure 11(c). The decrease in R/R_0 with k can be explained from the perspective of energy, since a larger k corresponds to more energy for carbonization of PI, resulting in lower sheet resistance.

4 Conclusions

LIG was prepared by laser direct writing technology with the focus on characterizing the influence of laser parameters on the structure and sheet resistance of LIG. The microstructure of LIG changes from porous structure to fibrous bundles with the increase of laser power. Both thickness and expansion ratio increase with laser power. The expansion of LIG is very pronounced with the total thickness being several times the thickness of PI film. TEM observation shows that LIG is composed of many graphene layers with layer spacing of 0.34 nm, which is consistent with the layer spacing obtained from the XRD pattern by the Bragg formula. The specific surface area of LIG decreases with the increase of laser power. Laser power was found to have a great influence on the morphology, thickness, and sheet resistance of LIG. Laser processing parameters such as laser power, scanning speed, image resolution, scanning pass, and off-focus value all have significant effects on the sheet resistance of LIG. The smaller sheet resistance of LIG can be achieved under a larger laser power, a smaller scanning speed, a smaller off-focus value (absolute value), and a higher image resolution due to the larger energy consumed by PI. In addition, with the increase of laser radiation energy, the microstructure of LIG changes from porous to tighter fibrous structure, weakening its bending strain sensitivity. A second laser scan can make sheet resistance decrease significantly with little effect after three scanning passes due to the saturation of carbonization of PI. The superposition mechanism of adjacent laser spots can be used to explain the influence of image resolution and off-focus value on the energy consumed by PI and thus on the sheet resistance of LIG. The understanding of the influence of laser processing parameters on microstructure and electrical conductivity paves the way for the rational design of LIG-based flexible electronic devices with improved sensing performance and reduced energy consumption.

This work was supported by the National Natural Science Foundation of China (Grant No. 51705082), the State Key Laboratory of Digital Manufacturing Equipment and Technology, Huazhong University of Science and Technology (Grant No. DMETKF2021013). CHENG HuanYu acknowledges the supports provided by the National Science Foundation (NSF) (Grant No. ECCS-1993072), the American Chemical Society Petroleum Research Fund (59021-DNI7), the National Heart, Lung, and Blood Institute of the National Institutes of Health (Grant No. R61HL154215), and Penn State University.

1 Liu Y, Wu X, Zhao Y, et al. Half-metallicity in hybrid graphene/boron nitride nanoribbons with dihydrogenated edges. J Phys Chem C, 2011, 115: 9442–9450
2 Jeon I Y, Zhang S, Zhang L, et al. Edge-selectively sulfurized graphene nanoplatelets as efficient metal-free electrocatalysts for oxygen reduction reaction: the electron spin effect. Adv Mater, 2013, 25: 6138–6145
3 Tao L Q, Tian H, Liu Y, et al. An intelligent artificial throat with sound-sensing ability based on laser induced graphene. Nat Commun, 2017, 8: 14579
4 Schwierz F. Graphene transistors: Status, prospects, and problems. Proc IEEE, 2013, 101: 1567–1584
5 Stoller M D, Park S, Zhu Y, et al. Graphene-based ultracapacitors. Nano Lett, 2008, 8: 3498–3502
6 Balandin A A. Thermal properties of graphene and nanostructured carbon materials. Nat Mater, 2011, 10: 569–581
7 Nair R R, Blake P, Grigorenko A N, et al. Fine structure constant defines visual transparency of graphene. Science, 2008, 320: 1308
8 Olenych I B, Aksimentyeva O I, Monastyrskii L S, et al. Effect of graphene oxide on the properties of porous silicon. Nanoscale Res Lett, 2016, 11: 43
9 Pinto A M, Gonçalves I C, Magalhães F D. Graphene-based materials biocompatibility: A review. Colloids Surf B: Biointer, 2013, 111: 188–202

10 Geim A. Graphene: Status and prospects. Science, 2009, 324: 1530–1534
11 Chen G, Liu Y, Liu F, et al. Fabrication of three-dimensional graphene foam with high electrical conductivity and large adsorption capability. Appl Surf Sci, 2014, 311: 808–815
12 Bolotin K I, Sikes K J, Jiang Z, et al. Ultrahigh electron mobility in suspended graphene. Solid State Commun, 2008, 146: 351–355
13 Xia J, Chen F, Li J, et al. Measurement of the quantum capacitance of graphene. Nat Nanotech, 2009, 4: 505–509
14 Wu Z S, Ren W, Gao L, et al. Synthesis of graphene sheets with high electrical conductivity and good thermal stability by hydrogen arc discharge exfoliation. ACS Nano, 2009, 3: 411–417
15 Yang X, Cheng H. Recent developments of flexible and stretchable electrochemical biosensors. Micromachines, 2020, 11: 243
16 Chen K, Shi L, Zhang Y, et al. Scalable chemical-vapour-deposition growth of three-dimensional graphene materials towards energy-related applications. Chem Soc Rev, 2018, 47: 3018–3036
17 Sha J, Gao C, Lee S K, et al. Preparation of three-dimensional graphene foams using powder metallurgy templates. ACS Nano, 2016, 10: 1411–1416
18 Yan Z, Ma L, Zhu Y, et al. Three-dimensional metal-graphene-nanotube multifunctional hybrid materials. ACS Nano, 2013, 7: 58–64
19 Chen Z, Ren W, Gao L, et al. Three-dimensional flexible and conductive interconnected graphene networks grown by chemical vapour deposition. Nat Mater, 2011, 10: 424–428
20 Wu Z S, Winter A, Chen L, et al. Three-dimensional nitrogen and boron Co-doped graphene for high-performance all-solid-state supercapacitors. Adv Mater, 2012, 24: 5130–5135
21 Chabot V, Higgins D, Yu A, et al. A review of graphene and graphene oxide sponge: Material synthesis and applications to energy and the environment. Energy Environ Sci, 2014, 7: 1564–1596
22 Yang X, Cheng C, Wang Y, et al. Liquid-mediated dense integration of graphene materials for compact capacitive energy storage. Science, 2013, 341: 534–537
23 Tung V C, Allen M J, Yang Y, et al. High-throughput solution processing of large-scale graphene. Nat Nanotech, 2009, 4: 25–29
24 Bae S, Kim H, Lee Y, et al. Roll-to-roll production of 30-inch graphene films for transparent electrodes. Nat Nanotech, 2011, 5: 574–578
25 Cong H P, Ren X C, Wang P, et al. Macroscopic multifunctional graphene-based hydrogels and aerogels by a metal ion induced self-assembly process. ACS Nano, 2012, 6: 2693–2703
26 Luo S, Hoang P T, Liu T. Direct laser writing for creating porous graphitic structures and their use for flexible and highly sensitive sensor and sensor arrays. Carbon, 2016, 96: 522–531
27 Bobinger M R, Romero F J, Salinas-Castillo A, et al. Flexible and robust laser-induced graphene heaters photothermally scribed on bare polyimide substrates. Carbon, 2019, 144: 116–126
28 Zhang Y, Chen Y, Huang J, et al. Skin-interfaced microfluidic devices with one-opening chambers and hydrophobic valves for sweat collection and analysis. Lab Chip, 2020, 20: 2635–2645
29 Zhang L, Ji H, Huang H, et al. Wearable circuits sintered at room temperature directly on the skin surface for health monitoring. ACS Appl Mater Interfaces, 2020, 12: 45504–45515
30 Hogan N J, Urban A S, Ayala-Orozco C, et al. Nanoparticles heat through light localization. Nano Lett, 2014, 14: 4640–4645
31 Frame J W. Removal of oral soft tissue pathology with the CO_2 laser. J Oral Maxillofacial Surgery, 1985, 43: 850–855
32 Stensitzki T, Yang Y, Kozich V, et al. Acceleration of a ground-state reaction by selective femtosecond-infrared-laser-pulse excitation. Nat Chem, 2018, 10: 126–131
33 Yang L, Yi N, Zhu J, et al. Novel gas sensing platform based on a stretchable laser-induced graphene pattern with self-heating capabilities. J Mater Chem A, 2020, 8: 6487–6500
34 Lin J, Peng Z, Liu Y, et al. Laser-induced porous graphene films from commercial polymers. Nat Commun, 2014, 5: 5714
35 S A R, M S, De S, et al. Laser induced graphene with biopolymer electrolyte for supercapacitor applications. Mater Today: Proc, 2020, doi: 10.1016/j.matpr.2020.08.791
36 Chen Y, Xu J, Yang Y, et al. Enhanced electrochemical performance of laser scribed graphene films decorated with manganese dioxide nanoparticles. J Mater Sci-Mater Electron, 2016, 27: 2564–2573
37 El-Kady M F, Strong V, Dubin S, et al. Laser scribing of high-performance and flexible graphene-based electrochemical capacitors. Science, 2012, 335: 1326–1330
38 Gao W, Singh N, Song L, et al. Direct laser writing of micro-supercapacitors on hydrated graphite oxide films. Nat Nanotech, 2011, 6: 496–500
39 El-Kady M F, Kaner R B. Scalable fabrication of high-power graphene micro-supercapacitors for flexible and on-chip energy storage. Nat Commun, 2013, 4: 1475
40 Thekkekara L V, Jia B, Zhang Y, et al. On-chip energy storage integrated with solar cells using a laser scribed graphene oxide film. Appl Phys Lett, 2015, 107: 031105
41 Peng Z, Lin J, Ye R, et al. Flexible and stackable laser-induced graphene supercapacitors. ACS Appl Mater Interfaces, 2015, 7: 3414–3419
42 Rahimi R, Ochoa M, Yu W, et al. Highly stretchable and sensitive unidirectional strain sensor via laser carbonization. ACS Appl Mater Interfaces, 2015, 7: 4463–4470
43 Duy L X, Peng Z, Li Y, et al. Laser-induced graphene fibers. Carbon, 2018, 126: 472–479
44 Rahimi R, Ochoa M, Tamayol A, et al. Highly stretchable potentiometric ph sensor fabricated via laser carbonization and machining of carbon-polyaniline composite. ACS Appl Mater Interfaces, 2017, 9: 9015–9023
45 Nayak P, Kurra N, Xia C, et al. Highly efficient laser scribed graphene electrodes for on-chip electrochemical sensing applications. Adv Electron Mater, 2016, 2: 1600185
46 Zhang C, Xie Y, Deng H, et al. Monolithic and flexible ZnS/SnO_2 ultraviolet photodetectors with lateral graphene electrodes. Small, 2017, 13: 1604197
47 Wang X, Chen Y, Schmidt O G, et al. Engineered nanomembranes for smart energy storage devices. Chem Soc Rev, 2016, 45: 1308–1330
48 Ye R, Chyan Y, Zhang J, et al. Laser-induced graphene formation on wood. Adv Mater, 2017, 29: 1702211
49 Kim J, Jeon J H, Kim H J, et al. Durable and water-floatable ionic polymer actuator with hydrophobic and asymmetrically laser-scribed reduced graphene oxide paper electrodes. ACS Nano, 2014, 8: 2986–2997
50 Wang W T, Lu L S, Xie Y X, et al. One-step laser induced conversion of a gelatin-coated polyimide film into graphene: Tunable morphology, surface wettability and microsupercapacitor applications. Sci China Tech Sci, 2020, 64: 1030–1040
51 Sun B, McCay R N, Goswami S, et al. Gas-permeable, multifunctional on-skin electronics based on laser-induced porous graphene and sugar-templated elastomer sponges. Adv Mater, 2018, 30: 1804327
52 Wan Z, Nguyen N T, Gao Y, et al. Laser induced graphene for biosensors. Sustain Mater Technologies, 2020, 25: e00205
53 Huang L, Su J, Song Y, et al. Laser-induced graphene: En route to smart sensing. Nano-Micro Lett, 2020, 12: 157
54 Zhu J, Hu Z, Song C, et al. Stretchable wideband dipole antennas and rectennas for RF energy harvesting. Mater Today Phys, 2021, 18: 100377
55 Zhang C, Peng Z, Huang C, et al. High-energy all-in-one stretchable micro-supercapacitor arrays based on 3D laser-induced graphene foams decorated with mesoporous ZnP nanosheets for self-powered stretchable systems. Nano Energy, 2021, 81: 105609
56 Li X, Tang T, Li M, et al. Photochemical doping of graphene oxide thin films with nitrogen for electrical conductivity improvement. J Mater Sci-Mater Electron, 2015, 26: 1770–1775
57 Romero F J, Salinas-Castillo A, Rivadeneyra A, et al. In-depth study of laser diode ablation of kapton polyimide for flexible conductive substrates. Nanomaterials, 2018, 8: 517

58 Stankovich S, Dikin D A, Piner R D, et al. Synthesis of graphene-based nanosheets via chemical reduction of exfoliated graphite oxide. Carbon, 2007, 45: 1558–1565
59 Tuinstra F, Koenig J L. Raman spectrum of graphite. J Chem Phys, 1970, 53: 1126–1130
60 Ferrari A C, Meyer J C, Scardaci V, et al. Raman spectrum of graphene and graphene layers. Phys Rev Lett, 2006, 97: 187401
61 Vidano R P, Fischbach D B, Willis L J, et al. Observation of Raman band shifting with excitation wavelength for carbons and graphites. Solid State Commun, 1981, 39: 341–344
62 Wu D, Deng L, Mei X, et al. Direct-write graphene resistors on aromatic polyimide for transparent heating glass. Sens Actuat A-Phys, 2017, 267: 327–333
63 Peng Z, Ye R, Mann J A, et al. Flexible boron-doped laser-induced graphene microsupercapacitors. ACS Nano, 2015, 9: 5868–5875
64 Thommes M, Kaneko K, Neimark A V, et al. Physisorption of gases, with special reference to the evaluation of surface area and pore size distribution (IUPAC Technical Report). Pure Appl Chem, 2015, 87: 1051–1069
65 Kwon S, Yoon Y, Ahn J, et al. Facile laser fabrication of high quality graphene-based microsupercapacitors with large capacitance. Carbon, 2018, 137: 136–145
66 Duan X, Luo J, Yao Y, et al. A route toward ultrasensitive layered carbon based piezoresistive sensors through hierarchical contact design. ACS Appl Mater Interfaces, 2017, 9: 43133–43142
67 Zhang M, Tang K, Zhang J, et al. Effects of processing parameters on underfill defects in deep penetration laser welding of thick plates. Int J Adv Manuf Technol, 2018, 96: 491–501